
KB-PJX: A TIM-Mountable Streaked Imager Based on a Versatile X-Ray Microscope Coupled to a High-Current Streak Tube

Introduction

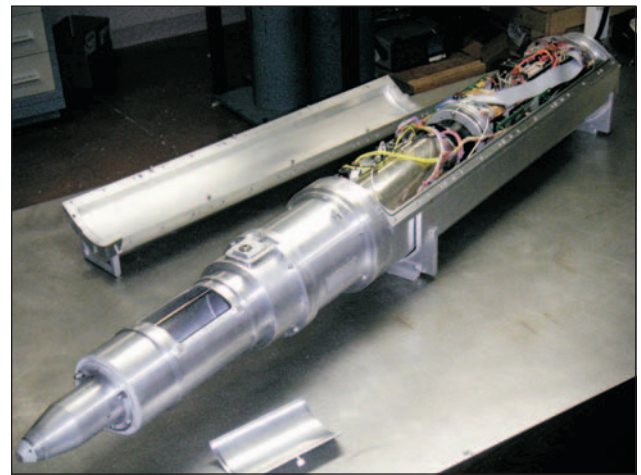
Experiments carried out on the OMEGA¹ laser place very stringent requirements on target-chamber diagnostics. For example, the development of early-time hydrodynamic instability measurements in inertial confinement fusion (ICF) targets involves x-ray radiographic techniques that require a diagnostic capable of detecting small perturbation amplitudes and high spatial frequencies. These are observed as variations in the areal density ρR :

$$\rho R(x, y; t) = \int_0^{d(x, y; t)} \rho(x, y, R; t) dR, \quad (1)$$

where, in the simple case of planar geometry, $d(x, y; t)$ is the target thickness (changing with time due to compression and ablation), x and y are the lateral coordinates, R is the coordinate along the diagnostic line of sight, and ρ is the evolving target density. A new x-ray diagnostic system (KB-PJX) has been developed, characterized, and fielded to measure small, high-spatial-frequency perturbations. It is re-entrant and can be mounted in any of the six OMEGA ten-inch manipulators (TIM's) arrayed around the target chamber, greatly increasing the available experimental configurations and reducing the time required for system adjustments.

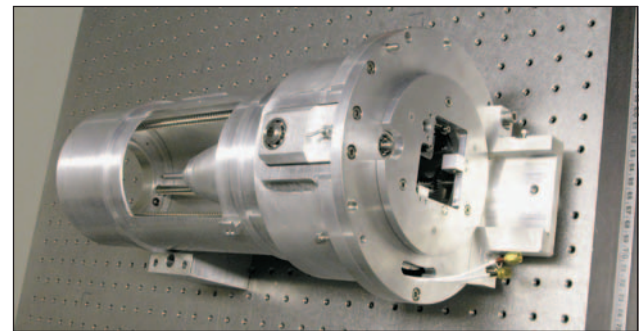
The KB-PJX is a streaked imager based on the advanced PJX streak tube and a modular optical front end built around a relatively simple Kirkpatrick–Baez² (KB) microscope design. It consists of two mechanically distinct modules (Fig. 99.49): the PJX air bubble that houses the streak tube, the CCD and the PJX electronics, and a retractor housing the optical front end. The retractor (Fig. 99.50) makes it easy to service the optics while mounted in a TIM (operations such as replacement of the blast shield protecting the mirrors are common). It also provides a reference base that allows for precise optical coupling of the front end to the PJX. A kinematic mount engages when the retractor is fully extended and provides repeatability in the optical alignment with a precision better than 25 μm . Another advantage of a retractor module

versus a more-permanent fixture is the possibility of replacing the default optical front end with another x-ray optic for some experiments. This design also provides a choice between single and multiple image modes, with the ability to dynami-



E13165

Figure 99.49
The KB-PJX diagnostic: the retractor in extended position and the PJX air bubble with the lid open.



E12907

Figure 99.50
Front-end retractor housing the KB microscope. The side cover is removed to expose the microscope cone.

cally reconfigure for either option with minimal effort. This extends the utility of the streak camera, making its speed, resolution, and collection efficiency available for a broad range of experiments.

The following sections describe/discuss (1) the optical front end and its basic features, design advantages, and expandability; (2) the optical characterization of the microscope in its default configuration; (3) the PJX detector; (4) the resolving capabilities (both spatial and temporal) of the full system; and (5) the performance of the imager in OMEGA hydrodynamic-stability experiments that required high-throughput, high-resolution x-ray diagnostic. Finally, a new technique for measuring the mass ablation rate, a key parameter of the dynamics of ICF implosions, is presented. This method takes advantage of the KB-PJX's ability to provide a continuous high-resolution record of the evolving target areal density.

Kirkpatrick–Baez (KB) Microscope

The relative simplicity and optical characteristics^{2,3} of a metal-coated KB x-ray microscope make it attractive for imaging high-temperature, laser-generated plasmas. Three implementations³ of x-ray KB microscopes mounted in the target chamber of the OMEGA laser facility¹ were available prior to this work. All of them were fixed at their respective locations. The instrument described in this article is designed for deployment in an OMEGA TIM—an air-lock device, used to insert diagnostics into the vacuum chamber. Six nearly orthogonal TIM's are available on OMEGA, providing positioning flexibility and rapid reconfiguration of instrumentation for experiments. The microscope serving as the front end of the KB-PJX is a large-grazing-angle ($\theta_i = 2.1^\circ$), four-mirror design (Fig. 99.51) that provides high throughput with a spatial resolution of less than $3 \mu\text{m}$ on axis.⁴ The relatively large angle of incidence increases the optic's solid angle ($\sim 3 \times 10^{-6}$ sr) and improves its resolution. The optimal resolution⁵ of a single mirror in the assembly scales as

$$d_{\text{opt}} \sim \left(\frac{p\lambda^2}{\theta_i} \right)^{1/3}, \quad (2)$$

where p is the object–mirror distance, λ is the x-ray wavelength, and θ_i is the grazing angle. Details of the optical design, choice of coating process, angle of incidence, and mirror characterization are given in Ref. 4. The mirrors have spherical concave surfaces with radii of curvature $R = 4250$ mm. The surface roughness and the optical figure have been measured

in Ref. 4 to be within the specified ranges. The surface roughness after coating was $\sim 4.4 \text{ \AA}$ rms, and the surface figure (deviation from the best-fit sphere) was measured through interferometry to be $< \lambda/40$ ($\lambda = 532$ nm). The radius of curvature is sufficiently large (compared to mirror thickness along the optical axis) that each mirror obeys the thin-lens equation

$$\frac{1}{f} = \frac{1}{p} + \frac{1}{q} = \frac{2}{R \sin(\theta_i)}, \quad (3)$$

where f is the focal distance and p and q are the object and image distances. For the KB-PJX geometry, $p = 90$ mm, $q = 560$ mm (magnification of about 6), and $f = 77.5$ mm. These distances are measured from the center of assembly (the contact plane of the perpendicular mirrors), making f an average value. The slight difference in focal distance for the front and back mirrors in a pair (which have different p 's and q 's) is compensated by a slight change in the incidence angle [see Eq. (3)].

The traditional method of assembling fixed KB x-ray mirrors is optical contacting, a technique yielding strength and longevity. This technique is not amenable to adjustment. Another option for mirror assembly is using special epoxy mixtures to glue the elements together, but any errors can be expensive to fix, especially when dealing with high-cost

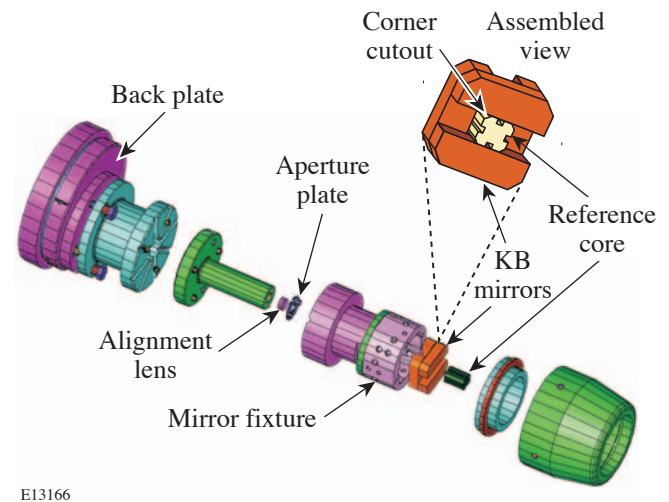


Figure 99.51

Assembled view of the microscope in the mounting mechanism. The mirrors are aligned against the reference core.

superpolished mirror elements. These methods provide robust assembly but limit the flexibility of the resulting optical systems, and fine-tuning their performance after assembly is difficult. The mechanical mirror mount used here allows for easy replacement or repositioning of the individual mirrors. Optimal mirror alignment is achieved by using a central reference core (the 10-mm-long, parylene-coated glass piece shown in Fig. 99.51) with the four Zerodur mirror elements pressed against it with ball plungers. The reference core is the most-unique feature of the optic's mechanical design. Its sides provide reference surfaces for the concave mirror faces, mitigating inaccuracies in the mirror element shape. The core was precisely machined to the specifications validated with numerical ray tracing. The assembly is built around a hollow Zerodur base. The front surface determines a reference plane along the optical axis and establishes the proper object distance for the microscope. An aluminum mirror fixture, mounted on this base as shown in Fig. 99.51, houses the mirror-core assembly and has screw holes for the ball plungers that provide fine mirror positioning and alignment by pressing each mirror against the reference core. Since Zerodur has one of the highest values for the Young's modulus ($E = 91$ GPa), available in a mirror material, the change of optical surface figure due to pressing stresses is not an issue. The estimated change in the surface figure, given the mirror element geometry and a maximum mounting force of 2.5 N is 0.7 nm, or about 20 times smaller than the acceptable surface figure. This assembly is resistant to vibrations and mechanical shocks associated with the operation of the TIM's. The rectangular profile of the central core provides for co-focusing of the mirrors in each imaging pair by introducing a small difference in the incidence angle (distance to optical axis) that compensates the difference in their position with respect to the object plane.³ The glass core baffles the direct x rays not participating in image formation and is coated with parylene to reduce x-ray scattering. Both 1-D (reflections from a single mirror) and 2-D (two-mirror reflection) imaging modes are available from apertures in the mounting core. This is accomplished with the rectangular side grooves that define an aperture for single-reflection x rays and corner cutouts, defining apertures for double reflection (Fig. 99.51). For experiments where the photon signal levels are low, the microscope can be configured for use in the 1-D imaging mode with a streak camera as a detector and benefit from the $1/R$ (R being the Ir coating reflectivity) increase in photon flux. Due to its relatively large solid angle,⁴ the optic can be used with streak cameras even in the 2-D mode, with the added benefit of precise spatial alignment in the target field of view. A special film pack that mounts to the back of the retractor mechanism and sits at the image plane (i.e., the PJX

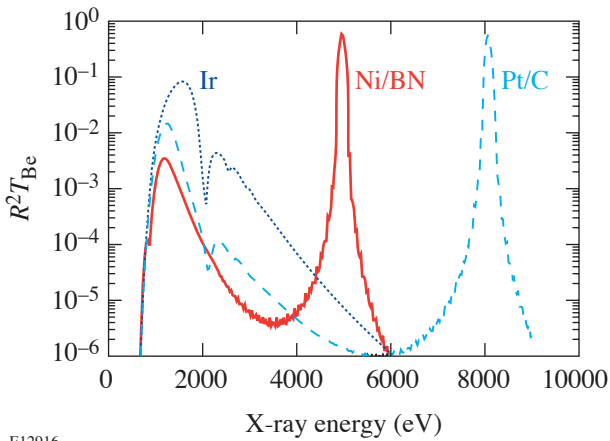
photocathode location) is available to optimize the fine alignment in 2-D object space. A thin (200- μm) Ta aperture plate at the back of the optic provides further baffling. The size and position of the apertures on the plate are determined by the mode of operation (1-D, 2-D, single or multiple images). By choosing the appropriate plate, one limits the x rays to those forming the desired image(s). The apertures are large enough not to act as pinholes (~ 0.5 mm on average) and are equivalent to field stops. This system of easily replaceable aperture plates and thick glass core, when combined with the mirror reflectivity cutoff, acts as an efficient filter for scattered, high-energy x rays that can lower image contrast. The mirror reflectivity is maximized by using superpolished mirror substrates, manufactured by Research Electro-Optics⁶ and iridium-coated at LLE. The quality of the deposited Ir film was verified by measuring the mirror's x-ray reflectivity at grazing incidence. By matching the measured reflectivity curve with that predicted by a numerical model,⁷ the film density was estimated to be about 98% of the bulk material density. Near-bulk (22.42-g/cm³) density of the iridium film is needed to achieve the optimal reflectivity that strongly depends on the electron number density. The film surface finish was characterized with an atomic force microscope (AFM). The measured surface roughness was used in the numerical fit to the reflectivity curve to determine the film density. With the Ir-coated mirrors in its current configuration, the microscope has a spectral window centered at about 1.5 keV with 0.4-keV FWHM. The finite width of the working energy band is provided by a Be blast shield, acting as a high-pass filter in combination with the cutoff in mirror reflectivity at the high-energy end. This cutoff can be estimated from the classical dispersion theory

$$E_c \sim \frac{he}{\theta_i} \sqrt{\frac{n_e}{\pi m_e}}, \quad (4)$$

where n_e is the electron density in the coating, m_e is the electron mass, h is Planck's constant, e is the electron charge (all units in cgs), and θ_i is the grazing angle in radians. For iridium, the total-reflection cutoff is $E_c \sim 2.36$ keV.

Replacing some or all of the mirror elements can extend or change the working energy band. To address different experimental requirements (an example is given later), the versatility of the KB-PJX will be extended by converting it into a high-photon-energy diagnostic with the addition of two new multilayer designs. These mirrors are designed to be drop-in replacements of the current metal-coated elements. The substrates are made with the same surface roughness and optical

figure as their soft-x-ray counterparts. They have the same geometric shape and work at the same angle of incidence. This simplifies the replacement of elements (or the whole assembly) and allows for dual band imaging, when multilayer and iridium-coated elements are mixed in the same assembly. Obtaining two simultaneous images from x rays in distinct energy bands can be very valuable in situations where large changes in the attenuation length occur within the field of view. The specifications of the new multilayer mirror elements are listed in Table 99.II, and their spectral response is compared to that of the soft-x-ray design in Fig. 99.52. The response is the product of the squared mirror reflectivity R^2 and the transmission through a standard 25- μm Be blast shield. The reflectivity cutoff E_c discussed above, along with the absorption edge at 1.56 keV of the Al debris filter, determines the narrow spectral window of the Ir-coated mirror assembly. The reflectivity is calculated with a numerical algorithm⁷ that uses the Fresnel equations and an analytic formula given by V. G. Kohn.⁸ In



E12916

Figure 99.52

Comparison of the spectral windows of two new multilayer (Ni/BN and Pt/C) assemblies (tuned to work at 4.95 keV and 8.05 keV) with the response of the current Ir-coated mirrors.

Table 99.II, d is the period (layer thickness) and d_1/d is the thickness ratio of the metal layer to the period. The last column lists the x-ray energies for which these mirrors are tuned. As with previous designs,^{9,10} the spectral windows of the multilayer elements are very narrow (<200-eV FWHM) since the Bragg condition $n\lambda = 2d \sin(\theta_i)$, determining the high reflectivity, is satisfied for a narrow band of wavelengths. This makes them good monochromators but limits the effective field of view of the optic by determining a preferential angle of incidence θ_i . A solution to this limitation is to use graded layer thickness across the mirror surface. Despite its complexity and higher cost, this method is now used routinely with good results.¹¹ This challenge can also be solved by using a sufficiently broadband backlighter and using the dispersive properties of the mirrors (a range of λ, θ_i pairs that satisfy the Bragg condition will exist). The field of view will then be expanded by angularly dispersing the signal in spatial direction. Since the efficiency of high-energy, broadband backlighters is low, a compound backlighter that emits in several spectral lines must be used. This results in discrete, spatially dispersed signal regions within the expanded field of view. For example, a brass backlighter [75% Cu ($K_a = 8048$ eV) and 25% Zn ($K_a = 8639$ eV)] is a good candidate for the 8-keV region. To register comparable intensity levels in the two spatial regions (which will map into the central 400 μm of the field of view), a two-strip Zn-Cu backlighter can also be used (Fig. 99.53).

Optic Characterization

After evaluating the reflectivity of each mirror,⁴ the mirror assembly was placed in the retracting mechanism that houses the microscope during normal operation and provides proper coupling to the PJX streak tube. Fine alignment and resolution evaluation were performed under vacuum in an x-ray test chamber. A film pack loaded with Kodak direct exposure film (DEF) was placed at the image plane where the PJX photocathode would be located during normal operation. Several test exposures were taken using a tungsten target bombarded with

Table 99.II: Characteristics of the new, multiplayer, high-energy KB-PJX mirrors.

Type	Layer	D (nm)	Thickness Ratio d_1/d	X-Ray Energy (keV)
Ni/BN	60	3.5	0.4	4.95
Pt/C	100	2.13	0.37	8.05

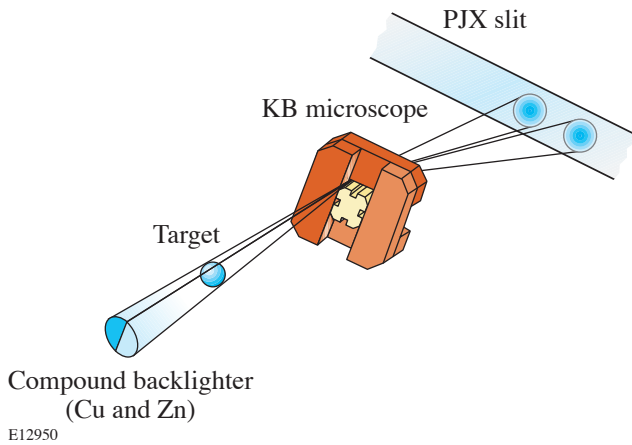


Figure 99.53
The field of view of a multilayer KB microscope is expanded by using a strip backlighter. The x rays are energy dispersed into two distinct regions at the image plane.

a 10-kV electron beam. Images of a 400-mesh grid as well as knife-edge images were acquired and analyzed to determine the system's modulation transfer function (MTF) and compare it with that predicted by numerical ray tracing⁴ and the MTF of an 8- μm -pinhole array. Figure 99.54(a) shows a typical film image of a 400-mesh grid, digitized with a Perkin-Elmer photodensitometer with a 5- μm scanning aperture. A horizontal lineout through the image is shown in Fig. 99.54(b), where the profile was intensity converted using a semi-empirical formula¹² in the instrument spectral window centered around 1.5 keV. The MTF was calculated from both the grid images and an image of an opaque tantalum foil edge (knife edge). The edge response function (and the MTF, respectively) is treated independently for the two perpendicular directions determined by the grid lines. The MTF shown in Fig. 99.55 is averaged over the central 200 μm of the field of view and calculated by a method similar to that outlined in Ref. 3. After taking into account the system magnification $M = 6$, the diffraction MTF predicted by numerical ray tracing⁴ was plotted on the same graph for comparison. It matches the shape of the edge MTF remarkably well. The slight deviations are most likely due to uncertainties in the determination of the line spread function from the edge data. It should be noted that the availability of a larger shadow region on the edge image provides for a more-accurate estimate of the transfer function for high spatial frequencies. Three MTF curves calculated from the edge image (for three different field positions) are shown on Fig. 99.56, along with the on-axis MTF of an 8- μm pinhole for comparison. In the central 600 μm of the field of view, the microscope has higher resolution than the pinhole. One can

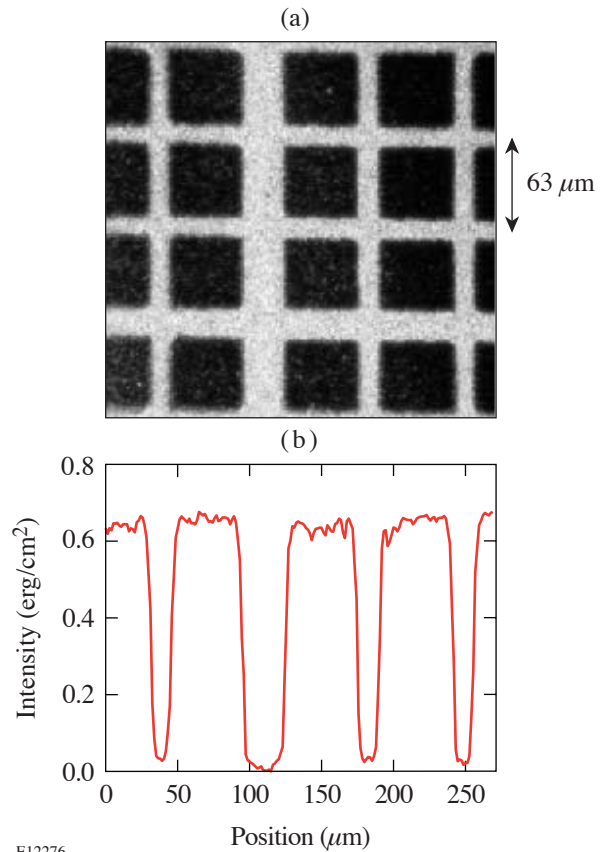


Figure 99.54
Film image (a) of a 400 LPI SEM grid and horizontal intensity profile (b) taken through the middle of it.

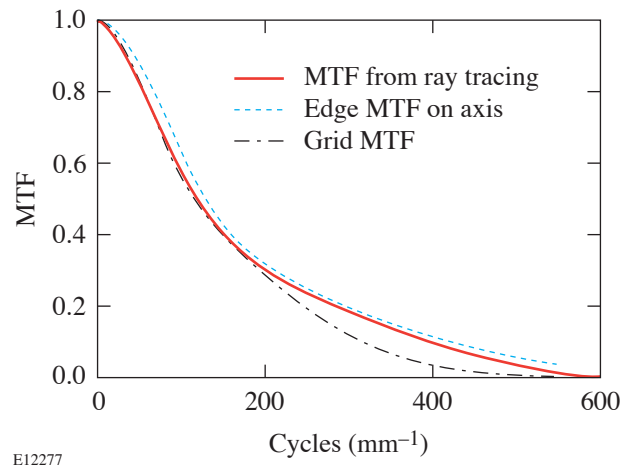


Figure 99.55
Modulation transfer function calculated from a grid image and vertical (perpendicular to the streak tube slit) knife edge.

also see the expected deterioration of resolution toward the edge of the field of view, where the resolution is comparable to the 8- μm pinhole.

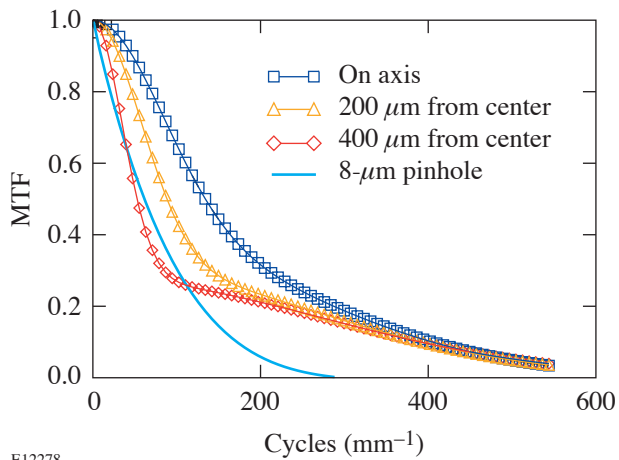


Figure 99.56 Modulation transfer functions calculated from an edge image at three different field positions are compared to the MTF of an 8- μm pinhole at a comparable magnification of 8 \times .

PJX Streak Tube

The instrument’s detector combines several state-of-the-art features that were previously not combined into a single detector. The PJX streak tube is the result of collaboration between the Commissariat à l’Énergie Atomique (CEA), Photonis (formerly Philips Photonique, located in Brive, France), and LLE. The final electron-optics design was completed by LLE. The streak tube is physically large—13 cm in diameter and 50 cm long. The camera is routinely operated with a 15-kV cathode–anode potential that can be increased to

25 kV. A quadrupole doublet, combined with three octupole correctors that minimize the aperture aberrations, focuses the accelerated photoelectrons. The phosphor screen is fiber-optic–coupled directly to a back-illuminated CCD and has a 24-mm \times 24-mm output format. The CCD has a 13.5- μm individual pixel size. The system gain¹³ is 150 CCD electrons per streak-tube electron, enabling single-electron detection with a signal-to-noise ratio (SNR) >3. There is no image intensifier in the camera, eliminating an additional source of noise. The streak tube can operate in either of two modes, determined by the polarity of the quadrupole doublet: in standard mode, the input slit size is 60 mm by 0.4 mm, with a demonstrated current-handling capability of 12.5 mA, while in inverse mode, the effective slit size is reduced to 6 mm by 0.09 mm with 1.5-mA peak current. In standard mode, the electron-optic spatial magnification is 0.4 \times and the temporal is 4 \times . Switching to inverse mode reverses the spatial and temporal direction magnifications. The streak tube is designed to mount in the OMEGA TIM enclosed in its own air bubble that houses the tube and the water-cooled CCD camera. The power, control, and communication electronics are internal to the air bubble, making the PJX a highly integrated self-contained instrument (Fig. 99.57). Cooling the CCD camera and power electronics that must operate inside the vacuum chamber is simplified by this design. A fan drives air circulation inside the bubble, and the heat is extracted through a chilled-water line. Communication to and from the camera is via an optical fiber. The PJX is a heatsink, not a heat source, inside the vacuum chamber. Other advantages of the air-bubble concept are better electromagnetic interference (EMI) shielding, the freedom to use vacuum-incompatible materials for high-voltage insulation, and the protection of many serviceable components from DT contamination.

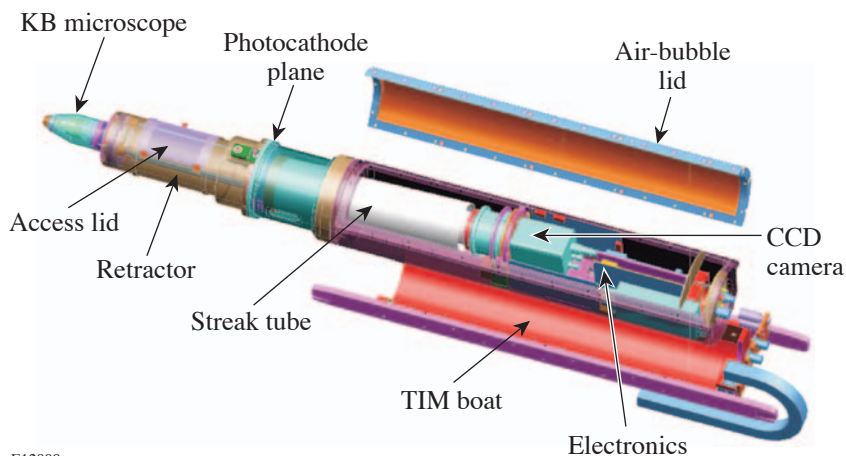


Figure 99.57 The PJX streak camera is kept at air in a “bubble” (shown with the lid open). This simplifies the cooling of both the CCD and power electronics.

E12909

The calculated time resolution of the PJX tube is less than 5 ps. The finite width D of the line spread function divided by the sweep speed v_{swp}

$$\Delta t_{\text{st}} = \frac{D}{v_{\text{swp}}} \quad (5)$$

is one of the primary factors that determine this.

For the inverse mode and an 8-ns sweep, Δt_{st} is 16-ps FWHM; it is proportionally less for faster sweep speeds. The energy dispersion of the secondary photoelectrons creates a spread in the transit time of the accelerated electrons,

$$\Delta t_{\epsilon} = f[V(z), \vec{v}_0, x_0, y_0], \quad (6)$$

where $V(z)$ is the axial potential, \vec{v}_0 is the initial velocity vector of the secondary electrons, and (x_0, y_0) is the initial point of emission. Δt_{ϵ} has been calculated to be 1.26 ps on axis for the KBr photocathode, increasing to 3.0 ps for the extreme off-axis locations. Assuming Gaussian response curves, the FWHM of the combined temporal line-response function will then be given as the Gaussian convolution of the two effects:

$$\Delta t \cong \sqrt{\Delta t_{\text{st}}^2 + \Delta t_{\epsilon}^2} \cong 16 \text{ ps}. \quad (7)$$

This value ($\Delta t \sim 16$ -ps FWHM) well represents the measured temporal resolution of the PJX in inverse mode. The number of time-resolution elements in the time window is ~ 300 , based on a 50% contrast-ratio criterion.

It is currently difficult to measure the time-resolution limit of the PJX because of the lack of sufficiently short x-ray pulses at LLE. The resolution calculated in Eq. (7) was verified using 100-ps laser pulses available on OMEGA. A train of six 100-ps Gaussian, UV pulses separated by 1 ns illuminate a U backlighter to produce the x-ray pulses shown in Fig. 99.58(a) (recorded in inverse mode). Except for the first x-ray pulse, two overlapped OMEGA beams were used to generate each of the pulses. There are small aberrations away from the optical axis (center of the image), due to the spherically curved phosphor screen. This effect is characterized and corrected with an image-processing algorithm. A spatial average of the third x-ray pulse is shown in Fig. 99.58(b), along with the UV pulse that generated it. The time axis is calibrated, using a train of eight UV fiducial pulses fed into the camera with a fiber and recorded at the edge of the photocathode. The solid curve is the actual x-ray pulse, convolved with the time response (line-spread function) of the PJX. It provides a measure of the streak

camera's time resolution. The only other information currently available is the shape (dashed curve) of the UV laser pulse that generated the x rays; however, the time resolution of the P510 streak camera (that recorded those) is of the order of the calculated PJX resolution. Using the UV pulse information is further complicated by the time history of the conversion of UV light to x rays. A phenomenological x-ray-conversion formula, such as that from Ref. 14, can be used to relate the intensity I_{UV} of UV light with the converted x-ray intensity I_x , using a power law $I_x \propto I_{\text{UV}}^{\gamma}$. With a value of $\gamma \sim 3.4$ as determined in Ref. 14 and using the FWHM $D_{\text{UV}} = 109$ ps of the recorded UV backlighter pulse, the σ parameter of the x-ray-converted UV Gaussian $I_x(t) \sim \exp[-(t-t_0)^2 / (2\sigma_{\text{UV},x}^2)]$ is given by

$$\sigma_{\text{UV},x} = \frac{\sigma_{\text{UV}}}{\sqrt{\gamma}} = \frac{D_{\text{UV}}}{2\sqrt{2\gamma \ln(2)}} \cong 25.1 \text{ ps}. \quad (8)$$

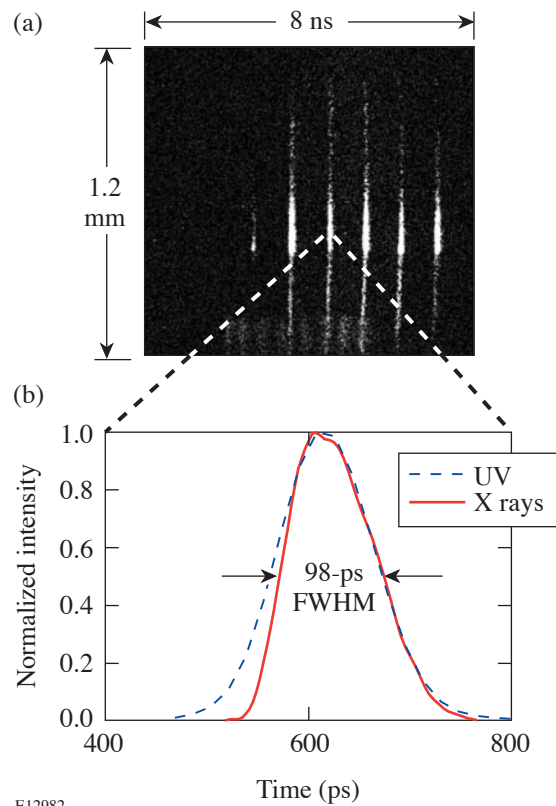


Figure 99.58 (a) A train of short backlighter pulses (100 ps) recorded with the KB-PJX in inverse mode and (b) spatial average of one such pulse and the generating UV pulse (dashed line).

The measured x-ray-intensity profile is fit by a combination of a Gaussian and an exponential decay function to account for the emission of x rays during the finite cooling time of the plasma. In Fig. 99.58(b), one can clearly see the asymmetry of the pulse due to this effect. The σ value of the Gaussian is found from the fit to be $\sigma_x = 32$ ps. Because this pulse is a convolution of the PJX time-response function with the incident x-ray pulse, the width of the time-response function is

$$\sigma_{\text{PJX}} = \sqrt{\sigma_x^2 - \sigma_{\text{UVx}}^2} \cong 19.8 \pm 4.0 \text{ ps}, \quad (9)$$

where the main contribution to the uncertainty comes from the determination of the power index γ . This result is consistent with Eq. (7).

The point-spread function (PSF) of the PJX streak camera in inverse mode has been measured to be $\sim 18 \mu\text{m}$ (versus $125 \mu\text{m}$ in standard mode) at the photocathode plane. This suggests that the camera and microscope will have a comparable effect on the resolution limit at the system magnification of $6\times$. The total point-spread function is a convolution of the two similar PSF's; therefore the resolution limit of the full instrument is expected to increase by a factor of $\sqrt{2}$ from the microscope resolution of $3 \mu\text{m}$ to $4.5 \mu\text{m}$. The magnification of the electron optics is $4\times$, resulting in a total magnification of $24\times$ to the CCD plane. The sharp edge of a Pt foil was imaged to measure the MTF of the complete KB-PJX system. The resulting MTF curve, as calculated from the edge data, is shown in Fig. 99.59. The curve was averaged over several time slices to improve the signal-to-noise ratio. For comparison, the

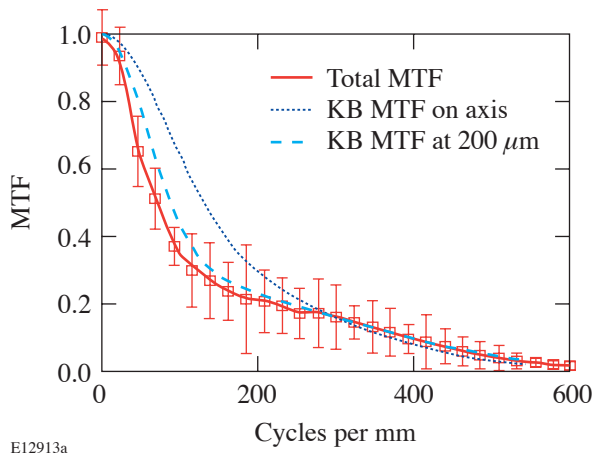


Figure 99.59
System MTF of the KB-PJX, calculated from its edge-response function and compared to the microscope MTF's at two field positions.

MTF's of the microscope, calculated on axis and $200 \mu\text{m}$ away from it, are plotted. It was verified from the target-positioning images that the edge was located 150 to $200 \mu\text{m}$ off axis, which explains the good match between the edge MTF and the microscope curve at $200 \mu\text{m}$ from the center. The expected $\sqrt{2}$ widening of the system PSF as compared to the optic's alone is detectable in this comparison. In this configuration the KB-PJX was used in a series of hydrodynamic stability experiments¹⁵ requiring high throughput (thick CH targets were driven with ten OMEGA beams) and high resolution. The instrument provided a continuous record of the evolving single-mode (typical wavelengths of $20 \mu\text{m}$) areal-density perturbations at the ablation front of these targets.

OMEGA Experiments

This KB optic coupled to the PJX streak camera has been used successfully to measure the time evolution of the areal density of a perturbed planar target during shock transit (prior to the arrival of the rarefaction wave at the laser-illuminated surface). A sinusoidal perturbation is imposed on the side of the target illuminated by the laser. The goal of the experiment is to measure the evolution of the perturbations and to compare it to various models. A continuous record of the evolution of target areal density (modulated by the ablation-front mass perturbations) was obtained (Fig. 99.60), showing phase inversion in the single-mode perturbations as part of a period of their oscillatory evolution. The temporal oscillations at the laser-illuminated surface are faster for mass perturbations with a shorter wavelength. The oscillation frequency is given by¹⁵

$$\omega = kV_a \sqrt{\rho_a / \rho_{\text{bl}}}, \quad (10)$$

where k is the spatial modulation wave number, ρ_a and ρ_{bl} are, respectively, the densities in the shock-compressed and blowoff plasma regions, and V_a is the ablation velocity (defined as the mass ablation rate divided by the density ρ_a). This sets challenges for the diagnostics since one has to go to shorter wavelengths to observe a full oscillation before rarefaction breakout, when the onset of the Rayleigh–Taylor instability overpowers the oscillatory stabilization effect. Several limitations make a simple increase of the target thickness (i.e., shock transit time) impractical; these include (1) limits in backlighter photon flux, laser pulse duration (total energy) of the backlighter, and drive beams; and (2) limits in the target modulation depth driven by the requirement to have the single-mode perturbation amplitude much smaller than its wavelength in order to remain in the linear regime of evolution, etc. All of these factors are interdependent, restricting the parametric

space of the experiment. The KB-PJX, having both high spatial resolution and high throughput, is the appropriate diagnostic for these experiments. Compared to a previous experiment on the subject,¹⁶ where part of an oscillation period for perturbation modes with wavelengths down to 30 μm was observed, the use of the KB-PJX allowed registering the evolution of perturbations with 20- and even 10-μm wavelengths, at the same target thickness and backlighter of equal or lower efficiency. In the experiments, CH targets were driven by ten of OMEGA’s ultraviolet beams with a maximum intensity of 4×10^{14} W/cm² on target in a 1.5-ns, fast-rise, flattop pulse. They were backlit with x rays produced by a U target, illuminated by another 11 OMEGA beams for 2 ns. A 25-μm-thick Be blast shield filtered the x-ray self-emission from the CH foils. The backlighter and target were separated by a 5-μm-thick Al debris shield, whose transmittance along with that of the Be foil and energy-dependent mirror reflectivity forms the working energy band, as shown in Fig. 99.52. The backlighter and driver pulse widths were chosen so that the camera registered the target areal density for the duration of the shock transit, up to the arrival of the rarefaction wave at the front of the compressed target. The streaked images, such as the one in Fig. 99.60, allow us to verify the theoretical models and validate the capabilities of the imager. The streaked microscope met its resolution and throughput requirements, making it possible to measure the perturbation oscillations.¹⁵ Resolution estimates from recorded data confirm that the imager can resolve modulations with a characteristic wavelength of 5 to 7 μm and an optical depth above 0.05 (about twice the typical noise level). Currently, the optic is also being used together with the PJX streak tube in the development of a side-on radiographic technique¹⁷ for equation-of-state (EOS) experiments.

Mass-Ablation-Rate Measurements with the KB-PJX

The ability of the KB-PJX to provide a continuous temporal record (with high time resolution) of the target’s optical depth can be used in a novel technique to measure the time evolution of the mass ablation in an ICF target. The level of self-emission of the ablated hot plasma in a CH target driven by ten of OMEGA’s beams was measured without backlighting, using only the x rays emitted from its hot corona and attenuated through the remainder of the target. The measured intensity profile I_{SE} is shown in Fig. 99.61 along with the time history I_{BL} of an undriven, backlit target and one from a target that is both driven and backlit. Due to ablation, the backlighter x rays see less optical depth at later times since the ablated material loses its opacity rapidly by heating up as it moves along the temperature gradient, away from the ablation front. The hot, low-density corona is approximately transparent to the 1.5-keV x rays up to the ablation front, where the largest temperature jump occurs. In time, the growing ablated mass reduces the total areal density of the target. Figure 99.61 shows an increasing difference between the intensity I_D from the backlit and driven target (red curve) and the sum $I_{SE} + I_{BL}$ (blue curve) of intensities from the driven-only and backlit-only foils. Measuring the optical-depth evolution of the target material not yet ablated allows the mass-ablation rate to be inferred. Consider these three intensity terms as functions of time:

$$I_{BL}(t) = I_{BL}^0(t)e^{-\mu_0 \rho_0 d_0} = I_{BL}^0(t)e^{-\mu_0 m_0} \quad , \quad (11)$$

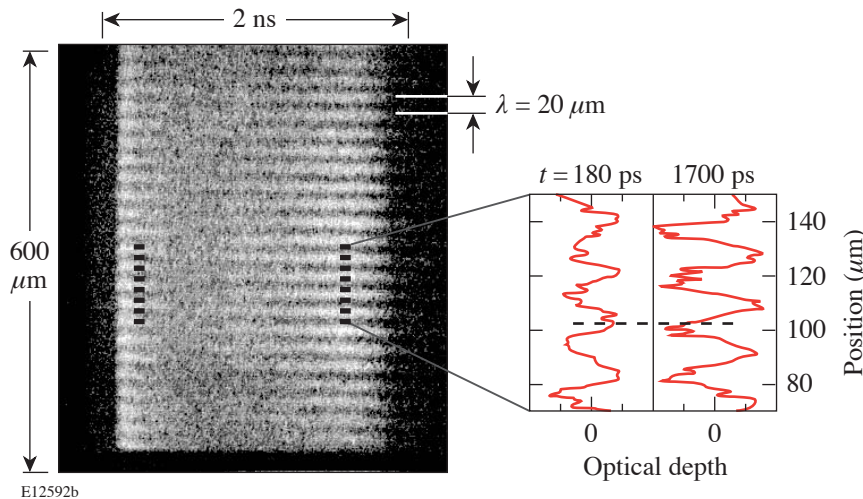


Figure 99.60
Streaked image of directly driven planar CH target with 60-μm thickness and single-mode ($\lambda = 20 \mu\text{m}$) surface modulations on the front. Spatial profiles are shown at $t = 180$ and 1700 ps, respectively.

$$I_D(t) = I_{SE}(t) + I_{BL}^0(t) e^{-\mu_0(m_0 - \rho_0 U_s t) - \mu_c \left(\rho_0 U_s t - \int_0^t \dot{m} dt' \right)}. \quad (12)$$

In Eq. (12) the spectrally weighted mass absorption coefficient μ_c in the compressed region (in the second exponential term) is assumed to change very little from its uncompressed-target value μ_0 . The other approximation made in Eq. (12) is that the optical depth $\mu_{abl} m_{abl}$ of the ablated material is negligible (due to its low opacity). Both assumptions are supported by data from the 14000-group APL opacity tables,¹⁸ for density and temperature profiles in the compressed and ablation regions, obtained from 1-D hydrodynamic simulations. Solving the last equation for the ablation rate yields

$$\dot{m}(t) = \frac{d(\Delta OD)}{\mu_0 dt} = - \frac{d \left[\ln \frac{I_D(t) - I_{SE}(t)}{I_{BL}(t)} \right]}{\mu_0 dt}. \quad (13)$$

All of the intensities are measured and μ_0 —the mass absorption coefficient of the cold target—is also readily available. Even though the various intensities are measured in different shots, the results can be combined to estimate the mass ablation rate. The growing optical depth ΔOD of the ablated mass is shown in Fig. 99.62. Due to the intensity-pulse-shape dissimilarities, it is reasonable to get an average value of the time-dependent mass-ablation rate by fitting ΔOD with a straight line and determining its slope. The slope as determined from the fit is 0.77 ns^{-1} . Using the spectrally averaged attenuation length $\lambda = 12 \text{ }\mu\text{m}$ and the density of cold CH $\rho_0 = 1.06 \text{ g/cm}^3$ to obtain $\mu_0 = (\rho_0 \lambda)^{-1}$, one finds the ablation rate to be $\sim 0.98 \text{ mg/(cm}^2 \text{ ns)}$, in line with the average value obtained from simulations, using the measured pulse shapes. A more-precise experiment can be performed if a single shot is used to record both I_D and I_{BL} , while eliminating the target self-emission. This can be done if a high-energy backlighter is used in combination with the multilayer mirrors discussed in the **Kirkpatrick–Baez (KB) Microscope** section (p. 184). At 5 keV, for example, both the thicker target and the microscope’s spectral window will filter out the soft-x-ray self-emission. A thicker target will be used since target thickness must be comparable to the spectrally weighted attenuation length (cold material) for maximum sensitivity to ablation. If

the ablating target does not occupy the entire field of view, the intensity of the unattenuated backlighter can be recorded at the same time by recording part of the backlighter beam directly. This will allow the calculation of the mass-ablation-rate evolution curve from a single shot.

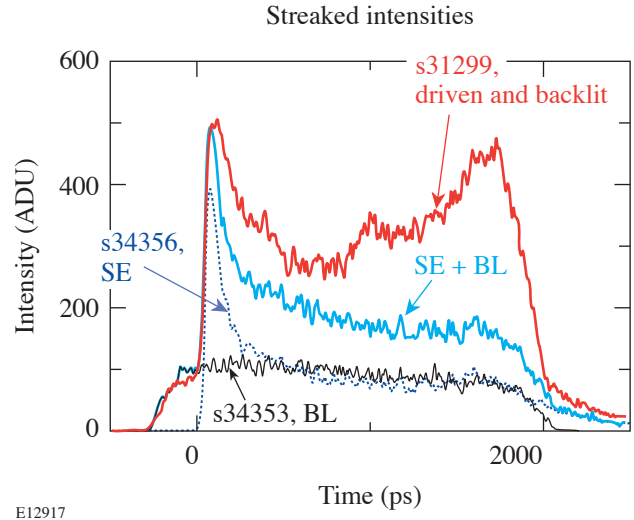


Figure 99.61

Intensity profiles of x rays transmitted through a 40- μm -thick CH target, which is driven and backlit (red curve), backlit only (black curve), and driven only (dotted curve). The sum of the thin solid and dotted lines (blue curve) does not match the solid, showing the effect of ablation.

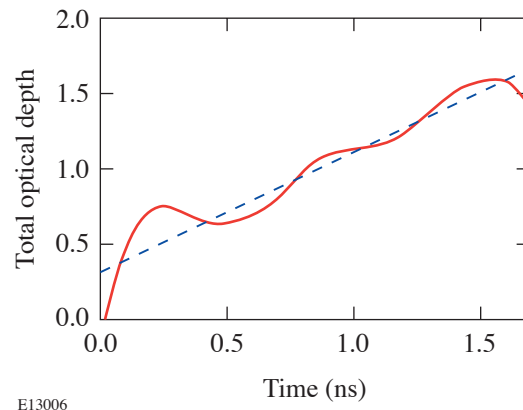


Figure 99.62

The difference in optical depth (ΔOD) (solid curve) grows due to mass ablation. An average value of the mass ablation rate is obtained by fitting the data with a straight line.

Conclusions

This article, in combination with Ref. 4, has shown that the KB-PJX is a versatile instrument, well suited for ICF experiments that (1) need a high-throughput diagnostic with high temporal and spatial resolution in x-ray radiography configurations and (2) can be set up for different x-ray-energy ranges. The imager has high temporal (less-than-20-ps) and spatial (better-than-5- μm) resolution in inverse mode, while demonstrating high-current-handling capabilities, matching the throughput of the optical front end. The PJX streak tube has met the experimental requirements, matching or surpassing the projected spatial ($\sim 18\text{-}\mu\text{m}$) and temporal ($< 20\text{-ps}$) resolution, while delivering high peak current in both modes of operation.

ACKNOWLEDGMENT

One of the authors (O. V. Gotchev) wishes to thank Dr. R. S. Craxton for his valuable comments on the opacity of CH plasma at various temperatures and densities. This work was supported by the U.S. Department of Energy Office of Inertial Confinement Fusion under Cooperative Agreement No. DE-FC52-92SF19460, the University of Rochester, and the New York State Energy Research and Development Authority. The support of DOE does not constitute an endorsement by DOE of the views expressed in this article.

REFERENCES

1. T. R. Boehly, D. L. Brown, R. S. Craxton, R. L. Keck, J. P. Knauer, J. H. Kelly, T. J. Kessler, S. A. Kumpan, S. J. Loucks, S. A. Letzring, F. J. Marshall, R. L. McCrory, S. F. B. Morse, W. Seka, J. M. Soures, and C. P. Verdon, *Opt. Commun.* **133**, 495 (1997).
2. P. Kirkpatrick and A. V. Baez, *J. Opt. Soc. Am.* **38**, 766 (1948).
3. F. J. Marshall and Q. Su, *Rev. Sci. Instrum.* **66**, 725 (1995); F. J. Marshall, M. M. Allen, J. P. Knauer, J. A. Oertel, and T. Archuleta, *Phys. Plasmas* **5**, 1118 (1998).
4. O. V. Gotchev, P. A. Jaanimagi, J. P. Knauer, F. J. Marshall, D. D. Meyerhofer, N. L. Bassett, and J. B. Oliver, *Rev. Sci. Instrum.* **74**, 2178 (2003).
5. G. R. Bennett, *Rev. Sci. Instrum.* **70**, 608 (1999).
6. Research Electro-Optics, Inc., Boulder, CO 80301.
7. E. M. Gullikson, Center for X-Ray Optics, Materials Sciences Division, E.O. Lawrence Berkeley National Laboratory, available at http://cindy.lbl.gov/optical_constants/; B. L. Henke, E. M. Gullikson, and J. C. Davis, *At. Data Nucl. Data Tables* **54**, 181 (1993).
8. V. G. Kohn, *Phys. Status Solidi B* **187**, 61 (1995).
9. J. H. Underwood and T. W. Barbee, Jr., *Appl. Opt.* **20**, 3027 (1981); J. H. Underwood, T. W. Barbee, Jr., and C. Frieber, *Appl. Opt.* **25**, 1730 (1986).
10. F. J. Marshall and G. R. Bennett, *Rev. Sci. Instrum.* **70**, 617 (1999).
11. Osmic, Inc., Auburn Hills, MI 48326.
12. B. L. Henke *et al.*, *J. Opt. Soc. Am. B* **3**, 1540 (1986).
13. S. Ghosh, R. Boni, and P. A. Jaanimagi, "Optical and X-Ray Streak Camera Gain Measurements," submitted to *Review of Scientific Instruments*.
14. F. J. Marshall, J. A. Delettrez, R. Epstein, R. Forties, R. L. Keck, J. H. Kelly, P. W. McKenty, S. P. Regan, and L. J. Waxer, *Phys. Plasmas* **11**, 251 (2004).
15. O. V. Gotchev, T. J. B. Collins, V. N. Goncharov, P. A. Jaanimagi, J. P. Knauer, and D. D. Meyerhofer, "Experiments on the Ablative Richtmyer-Meshkov Instability in Planar Direct-Drive Targets on OMEGA," to be submitted to *Physics of Plasmas*.
16. Y. Aglitskiy *et al.*, *Phys. Rev. Lett.* **87**, 265001 (2001).
17. L. B. Da Silva *et al.*, *Phys. Rev. Lett.* **78**, 483 (1997).
18. W. F. Huebner *et al.*, Los Alamos National Laboratory, Los Alamos, NM, Report LA-6760-M (1977).

